nature materials

LETTERS

https://doi.org/10.1038/s41563-021-01167-0

Check for updates

Moiré enhanced charge density wave state in twisted 1T-$TiTe_2$/1T-$TiSe_2$ heterostructures

Wei-Min Zhao[1,2,7], Li Zhu[1,2,7], Zhengwei Nie[3,4,7], Qi-Yuan Li[1,2], Qi-Wei Wang[1,2], Li-Guo Dou[1,2], Ju-Gang Hu[1,2], Lede Xian[5], Sheng Meng[3,4,5] ✉ and Shao-Chun Li[1,2,6] ✉

Nanoscale periodic moiré patterns, for example those formed at the interface of a twisted bilayer of two-dimensional materials, provide opportunities for engineering the electronic properties of van der Waals heterostructures[1–11]. In this work, we synthesized the epitaxial heterostructure of 1T-$TiTe_2$/1T-$TiSe_2$ with various twist angles using molecular beam epitaxy and investigated the moiré pattern induced/enhanced charge density wave (CDW) states with scanning tunnelling microscopy. When the twist angle is near zero degrees, 2×2 CDW domains are formed in 1T-$TiTe_2$, separated by 1×1 normal state domains, and trapped in the moiré pattern. The formation of the moiré-trapped CDW state is ascribed to the local strain variation due to atomic reconstruction. Furthermore, this CDW state persists at room temperature, suggesting its potential for future CDW-based applications. Such moiré-trapped CDW patterns were not observed at larger twist angles. Our study paves the way for constructing metallic twist van der Waals bilayers and tuning many-body effects via moiré engineering.

When two layers of van der Waals materials are stacked with a twist angle or lattice mismatch, a moiré pattern is produced by the long wavelength periodic potential arising from the interlayer atomic registries. The moiré pattern is a promising means of engineering the atomic structure and/or energy band of van der Waals bilayers and thus enables the emergent phenomena that would otherwise not exist in the corresponding individual layers. Great effort has been devoted to the discovery of phenomena originating from the moiré effect[7–10], with works focused on Hofstadter's butterfly and the fractal quantum Hall effect in graphene superlattices[3,4], moiré modulated topological order[6], and the quantum trapping of excitons in semiconducting transition metal dichalcogenide (TMD) bilayers[11]. Precise control of the twist angle has also led to the discovery of strong correlation effects. As the twist angle θ nears the magic angle of ~1°, electron–electron correlation in bilayer graphene becomes prominent, so that various correlated electronic phases including unconventional superconductivity, strongly correlated insulators, magnetism and topological edge states have been unveiled[1,5,8–10].

Even though semimetallic TMD van der Waals monolayers often exhibit many-body physics, such as superconductivity[12], the CDW state[13] and the Mott insulating state[14], little is known to date about the moiré effect in twisted bilayers of semimetallic TMDs. In this work, we adopt molecular beam epitaxy (MBE) to directly construct twisted 1T-$TiTe_2$/1T-$TiSe_2$ heterostructures, monolayer 1T-$TiTe_2$ on top of bilayer 1T-$TiSe_2$, with various twist angles. By using scanning tunnelling microscopy (STM), we demonstrate that at small twist angles, the moiré pattern traps the CDW domain in the 1T-$TiTe_2$ monolayer and substantially enhances its transition temperature (T_{CDW}); however, at large twist angles, no CDW state was observed since no atomic reconstruction occurred. In this way, we successfully tuned the many-body effects, particularly the electron correlation, in metallic van der Waals monolayers through moiré engineering.

The 1T-$TiSe_2$ material is a CDW material with a 2×2×2 periodicity in the bulk[15]. However, 1T-$TiTe_2$, a sister material to $TiSe_2$, exhibits no CDW transition in the bulk and only a weak 2×2 CDW order in the monolayer due to a much stronger band overlap[16]. Figure 1a illustrates the structural schematics of the $TiTe_2$/$TiSe_2$ heterostructure synthesized by MBE (Methods and Supplementary Fig. 1). To obtain a high-quality $TiSe_2$ surface and to minimize the substrate's influence, bilayer $TiSe_2$ instead of a monolayer was grown prior to bilayer graphene (BLG)/SiC. The additional $TiTe_2$ monolayer was then deposited on top of the as-grown $TiSe_2$ surface. (For comparison, the data for monolayer $TiTe_2$ grown on monolayer $TiSe_2$ can be found in Supplementary Fig. 2.) This method enabled us to construct heterostructures with various twist angles between $TiTe_2$ and $TiSe_2$ (Fig. 1b,c). According to the microscopic STM characterizations, many of the $TiTe_2$/$TiSe_2$ heterostructures are distributed in a range of twist angles near ~0°, roughly within ~±2°, and a few at larger twist angles (Supplementary Fig. 3). The period of moiré patterns was found to depend on the twist angle. Therefore, such variance of local twist angles enables the investigation of moiré-pattern-dependent electronic structures of 1T-$TiTe_2$/1T-$TiSe_2$ heterostructures.

Figure 1d–f shows a set of typical STM images of the 1T-$TiTe_2$/1T-$TiSe_2$ heterostructures with different twist angles. The quality of our $TiTe_2$/$TiSe_2$ heterostructure is comparable to that of the $TiTe_2$ epitaxial monolayer[16] (Supplementary Fig. 4). The fast Fourier transform (FFT) images (the insets to Fig. 1d–f) quantitatively give the lattice periodicity of the top 1T-$TiTe_2$ monolayer relative to the underneath 1T-$TiSe_2$. Adopting the experimentally determined lattice constants and twist angles, moiré patterns based on the rigid model were simulated, as shown in Fig. 1g–i. More details about the determination of the twist angle can be found in Supplementary Figs. 5–7. At a twist angle θ of ~0.5° (Fig. 1d), a tessellation-like pattern can be identified in each moiré unit cell, which is composed of two types of triangular-shaped domains. Such a distinct pattern is

[1]National Laboratory of Solid State Microstructures, School of Physics, Nanjing University, Nanjing, China. [2]Collaborative Innovation Center of Advanced Microstructures, Nanjing University, Nanjing, China. [3]Beijing National Laboratory for Condensed Matter Physics and Institute of Physics, Chinese Academy of Sciences, Beijing, P. R. China. [4]School of Physical Sciences, University of Chinese Academy of Sciences, Beijing, China. [5]Songshan Lake Materials Laboratory, Dongguan, P. R. China. [6]Jiangsu Provincial Key Laboratory for Nanotechnology, Nanjing University, Nanjing, China. [7]These authors contributed equally: Wei-Min Zhao, Li Zhu, Zhengwei Nie. ✉e-mail: smeng@iphy.ac.cn; scli@nju.edu.cn

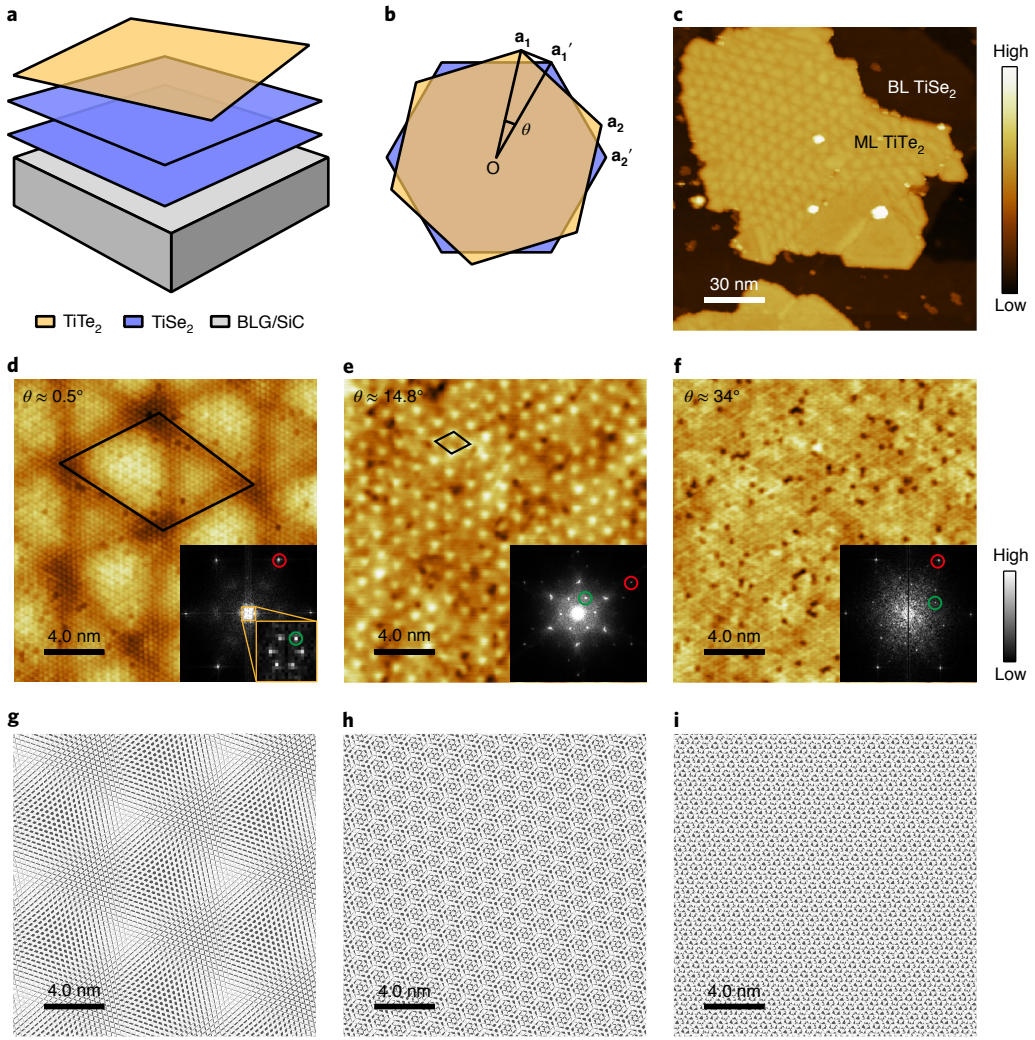

Fig. 1 | Evolution of the moiré pattern with twist angle for 1T-$TiTe_2$/1T-$TiSe_2$. **a**, Schematic of the vertically stacked $TiTe_2$/$TiSe_2$ heterostructure on a BLG/SiC(0001) substrate. **b**, Top view diagram of the $TiTe_2$/$TiSe_2$ heterobilayer with a twist angle θ. The $\mathbf{a}_1$ and $\mathbf{a}_2$ ($\mathbf{a}_1'$ and $\mathbf{a}_2'$) are the lattice vectors of the top (bottom) layer. **c**, Large-scale STM topographic image (150×150 nm^2, U=1.5 V, I_t=100 pA. U, bias voltage, I_t, tunneling current.) of the $TiTe_2$/$TiSe_2$ heterostructure with a near 0° twist angle. BL, bilayer; ML, monolayer. The colour bar in c represents the apparent height of the topographic images. **d**–**f**, STM topographic images of various moiré patterns with twist angles of 0.5°, 14.8° and 34°. The moiré supercell is marked by black solid lines. Insets, corresponding FFT images (size, 20×20 nm^2; **d**,**f**, U=+100 mV, I_t=100 pA; **e**, U=−300 mV, I_t=100 pA). The red and green circles mark the Bragg lattices of the $TiTe_2$ and moiré periods, respectively. The moiré period is associated with the low wavevector peak near the centre of the FFT. The coloured circles mark the real FFT peaks. The CDW points in the inset to **d** become faint and diffusive due to the loss of long-range coherence between the CDW tessellation domains. The colour bar in f represents the contrast of the FFT images. **g**–**i**, Rigid lattice moiré patterns (20×20 nm^2) simulated with twist angles similar to those of **d**–**f**, respectively.

in great contrast to the simulated rigid moiré pattern and indicates the atomic reconstruction resulting from the interplay between the interlayer van der Waals interactions and intralayer elastic strain, as usually occurs in the small-twist-angle regime of 2H-TMDs or graphene bilayers[5,17,18]. When the twist angle θ is away from 0°, atomic reconstruction becomes less prominent. For the cases of θ of ~14.8° and ~34°, as shown in Fig. 1e,f, the experimental patterns can be well reproduced by the simple unreconstructed twisted models, that is, continuously varying rigid moiré patterns (Fig. 1h,i).

Although structurally analogous to 2H-TMDs and graphene bilayers, new moiré properties are expected in these 1T-TMD heterostructures. We now focus on the moiré effect in the small-twist-angle regime. Figure 2a,b represents the high-resolution STM images of both unoccupied and occupied states taken on the moiré unit cell of θ of ~0.5°. In domain A, the apparently lower region as marked by the black triangle, a 1×1 hexagonal lattice at both occupied and unoccupied states is represented, corresponding to the top Te atoms of $TiTe_2$. However, in domain B, the apparently higher region as marked by the red triangle, a charge order is clearly identified. The FFT images of the separate domains B and A (Fig. 2c,d) and the line-scan profiles (Fig. 2e) show that the periodicity in domain B is twice that in domain A, suggesting a 2×2 CDW state in domain B. Thus, the moiré tessellation is composed of alternating 2×2 CDW (domain B) and 1×1 normal state (domain A) triangular domains, confined in the moiré unit cell. Of note, the distortion and apparent rotation of the moiré pattern is shown in Fig. 1c and in Supplementary Fig. 8, which is in fact due to the local variance of the twist angle, or the shear strain. The 2×2 CDW and 1×1 normal state tessellation are continuous throughout, indicating that they are robust over a range of small twist angles.

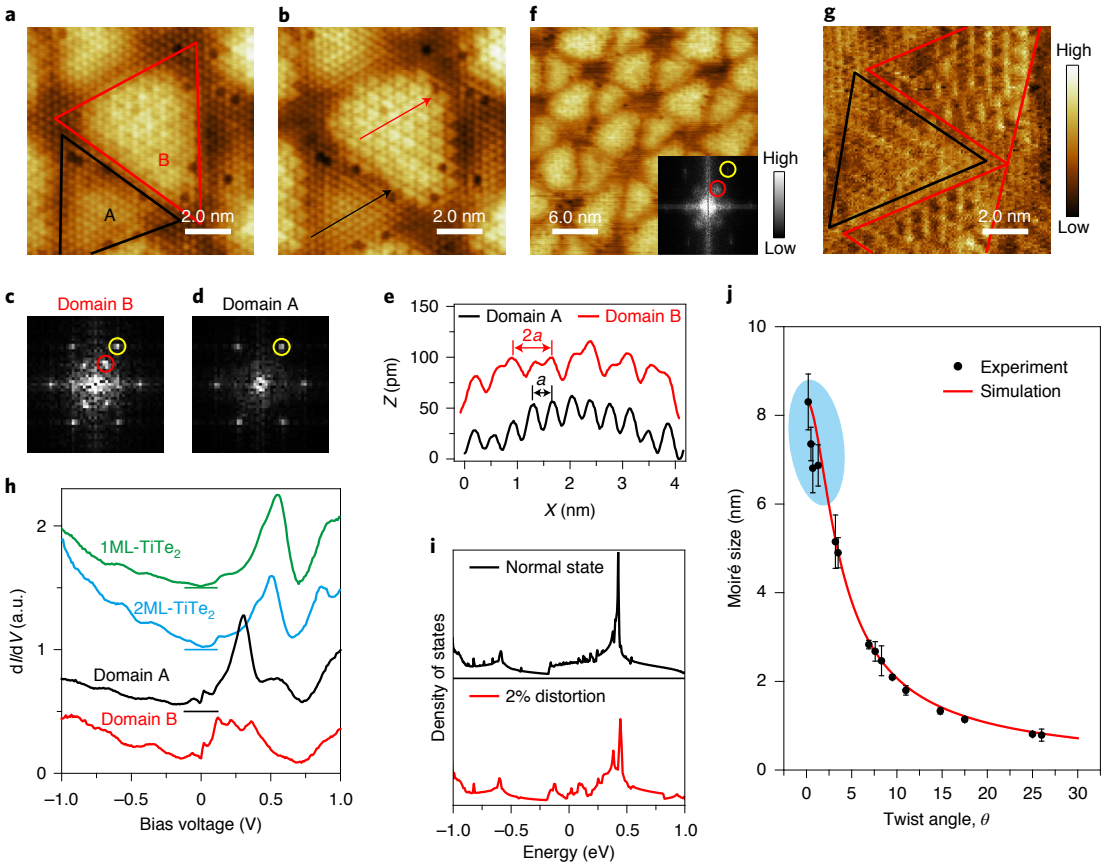

Fig. 2 | Strong CDW state confined in moiré pattern at twisted angle near 0°. a,**b**, High-resolution STM images of the empty state ($10\times10\,nm^2$, $U=+200\,mV$, $I_t=100\,pA$) and filled state ($10\times10\,nm^2$, $U=-200\,mV$, $I_t=100\,pA$) on the moiré unit cell with twisted angle θ of ~0.5°. The 1×1 normal state domain and 2×2 CDW state domain, marked by black and red triangles, are called domain A and domain B, respectively. **c**,**d**, FFT images of 2×2 CDW state domain and normal state domain. The yellow and red circiles mark the wave vectors for the 1×1 lattice and the CDW periodicity, respectively. **e**, Line-scan profile taken on the red and black lines in **b**. *a*, lattice constant of $TiTe_2$. *X*, length of the measured line-scan profile. *Z*, STM apparent height. **f**, Topographic image ($30\times30\,nm^2$, $U=+250\,mV$, $I_t=100\,pA$) of the moiré pattern at a twisted angle near 0° at room temperature. The inset shows the corresponding FFT image, and the 2×2 CDW periodic point is marked by a red circle. The colour bar in **f** represents the contrast of the inset FFT image. **g**, Zoomed-in current image of a moiré unit cell in **f**. The 1×1 normal state domain and 2×2 CDW state domain are marked by black triangles and red triangles, respectively. The colour bar in **g** represents the apparent height of the topographic images. **h**, Differential d*I*/d*V* spectra ($U=+0.5\,V$, $I_t=200\,pA$, $U_{mod}=10\,mV$. U_{mod}, voltage of the lock-in ac modulation.) taken on the $TiTe_2$/BLG and $TiTe_2$/$TiSe_2$ heterostructures. The green and blue curves represent the d*I*/d*V* spectra for monolayer and bilayer $TiTe_2$ on BLG/SiC(0001). The black and red curves represent the d*I*/d*V* spectra for the 1×1 and 2×2 domains in **a**. **i**, Computed density of states for single-layer $TiTe_2$ without (black line) and with (red line) Ti atomic displacement. **j**, Dependence of the moiré period on twist angle. The black filled circles with error bars were extracted from experimental data. The error bars are the standard deviation of moiré sizes measured in the STM image. The red curve represents the simulation result based on the rigid lattice models of $TiTe_2$/$TiSe_2$ and the function in Supplementary Note 1. The blue oval highlights the twist angle regions where the CDW tessellation states formed.

The moiré-trapped CDW state of $TiTe_2$ was also characterized at elevated temperature. Surprisingly, this CDW state can persist at room temperature, as indicated by the room temperature STM results (Fig. 2f,g). The 2×2 periodic points are marked by red circles in the corresponding FFT image (the inset to Fig. 2f). Furthermore, the zoomed-in image (Fig. 2g) for the moiré unit cell shows similar morphological details at room temperature as that at low temperature, that is, the 2×2 CDW state in domain B and the 1×1 normal state in domain A. We conclude that the T_{CDW} of this CDW state within the tessellation is above room temperature, which is much higher than that of the individual monolayer $TiTe_2$ of ~92 K (ref. [16]) and the bulk $TiTe_2$ where the CDW state is absent. The moiré pattern formed in the twisted heterostructure evidently plays a important role in enhancing the CDW transition in the monolayer $TiTe_2$ to above room temperature.

To further investigate the electronic structure of the moiré-trapped CDW and normal state, we performed scanning tunnelling spectroscopy (STS) measurements. Differential conductance (d*I*/d*V*; *I*, current; *V*, voltage) spectra, which represent the local density of states, were taken on the CDW state (domain B) and the normal state (domain A). The obtained d*I*/d*V* spectra, as depicted by the red and black lines in Fig. 2h, show a notable difference between the 1×1 normal state and 2×2 CDW state (spatially resolved spectra can be found in Supplementary Fig. 9). In the normal state domain, the spectrum mainly features a strong peak concentrated at ~+0.3 V in the unoccupied state (positive bias). This normal state spectrum looks almost the same as those taken of the individual $TiTe_2$/BLG/SiC monolayer or bilayer (the green and blue lines in Fig. 2h), regardless of the energy shift. The energy shift can usually be ascribed to the different interfacial charge transfers[19]. Even though a weak charge order was observed in the individual $TiTe_2$ monolayer (Supplementary Fig. 4b), its d*I*/d*V* spectrum shows no prominent difference from the $TiTe_2$ bilayer without a CDW transition or the normal state domain of

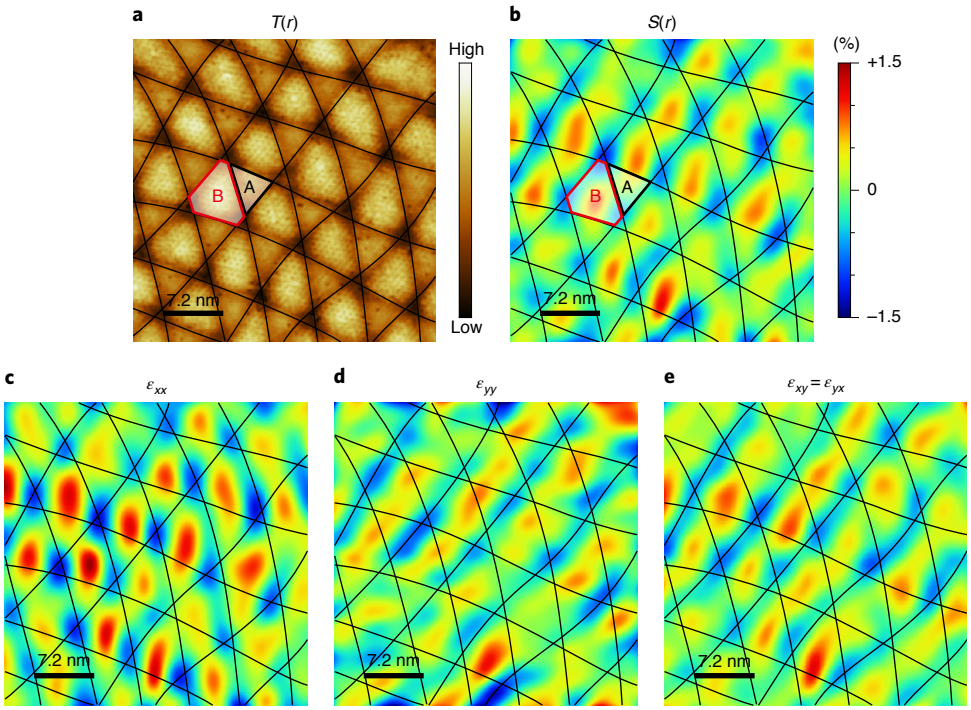

Fig. 3 | Distribution of the strain field in the moiré pattern near a 0° twist angle. a, STM topographic image (36×36 nm^2, $U=+100$ mV, $I_t=100$ pA) at a twist angle of ~1°. Black lines are guides to the eye for the moiré pattern, and the red hexagon marks a 2×2 CDW domain. $T(r)$ represents the STM apparent height at the location r. The colour bar in **a** represents the apparent height of the topographic image. **b**, Symmetric strain map $S(r)=(\varepsilon_{xx}+\varepsilon_{yy})/2$. $S(r)$ represents the symmetric strain at the location r. The colour bar in **b** represents the calculated value of strain. **c**,**d**, The ε_{xx} and ε_{yy} strain maps of the STM image **a** obtained by the geometric phase analysis method. **e**, Shear strain map $\varepsilon_{xy}=\varepsilon_{yx}$.

the tessellation, implying that its electronic structure is similar to the normal state. However, in the 2×2 CDW domain of the tessellation, the dI/dV characteristic peak near +0.3 V is weakened and split, and turns to a multipeaked feature. This multipeaked feature can be qualitatively reproduced by the density of states calculated by density functional theory (DFT) for a distorted CDW state of the $TiTe_2$ monolayer, as shown in Fig. 2i. The detailed calculation for the density of states and corresponding energy bands can be found in Supplementary Fig. 10. Thus, the CDW state in the tessellation hosts a true 2×2 band structure and is a strong charge order state, in contrast to the weak CDW state observed in the $TiTe_2$ monolayer. This strong charge order may also be responsible for the high T_{CDW} (greater than room temperature).

At other twist angles far away from 0°, where there is no atomic reconstruction and rigid moiré models can be applied, no CDW states were observed and the whole $TiTe_2$ monolayers were in the normal state, as shown in Fig. 2j and Supplementary Figs. 4e,f and 3 (part 2). Compared to the previously reported CDW superstructure in the $TiTe_2$ epitaxial layer on BLG/SiC (ref. [16]; our data in Supplementary Fig. 4), the absence of the CDW state at large twist angles may be due to electronic coupling from the underneath $TiSe_2$ (ref. [20]).

Considering that the CDW domain tessellation is present only in the small-twist-angle moiré patterns, and absent in large-twist-angle rigid moiré patterns, and that the CDW tessellation follows the moiré patterns at small twist angles, we conclude that the CDW and normal state tessellations are modulated/enhanced by the moiré pattern and that the small twist angle is important. Since CDW tessellation is always accompanied by local atomic reconstruction, the local strain effect originating from atomic reconstruction in the moiré pattern may play a decisive role in enhancing the CDW state.

Previous theoretical studies have reported that applying biaxial strain in $TiTe_2$ can narrow the semimetallic overlap and thus stabilize a 2×2 CDW distortion[21]. For the case of small-twist-angle $TiTe_2$/$TiSe_2$ heterostructures, atomic reconstruction, in turn, induces a local strain field. To verify whether the strain effect plays a role in enhancing the CDW state, the strain distribution was first carefully analysed via STM image (Fig. 3a) using geometrical phase analysis (GPA)[22,23]. The GPA-generated strain field distributions are represented by the strain tensor components ε_{xx} (Fig. 3c) and ε_{yy} (Fig. 3d; Supplementary Fig. 11 for more detail). The symmetric strain map $S(r)$, as defined by $S(r)=(\varepsilon_{xx}+\varepsilon_{yy})/2$ at the location r (ref. [24]), is shown in Fig. 3b. The strain in the CDW domain, as marked by the red truncated triangle in Fig. 3b, is found to be tensile and stronger than that in the normal state domain. Quantitatively, the statistics made over the surface give average values of ~+0.06% for domain A and ~+0.32% for domain B (Supplementary Fig. 12). To further characterize the possible shear strain, ε_{xy} was also calculated, as shown in Fig. 3e. Similar strain distributions have also been mentioned in the heterobilayers of graphene/hexagonal-boron-nitride and MoS_2/WSe_2 (refs. [25,26]). The strain distribution at large twist angles was also generated by GPA, as shown in Supplementary Figs. 13 and 14. By contrast, the obtained local strain field at large twist angles was nearly half an order of magnitude smaller than that at small twist angles.

To investigate the strain distribution in the moiré pattern further, we performed DFT calculations. Considering the computational expense, we constructed a $TiTe_2$/$TiSe_2$ moiré superlattice with a twist angle of ~1.7° to simulate the situation near 0°. Figure 4a shows the simulated heights of the top $TiTe_2$ layer relative to the bottom $TiSe_2$ layer. Evidently, the morphology of the top Te atoms shows a height undulation, with a lower region (domain A) and a higher region (domain B), as marked by black and red triangles, respectively. This agrees with the experimental results. We further defined the local strain as the relative change in the average distance between each Te atom and its six nearest

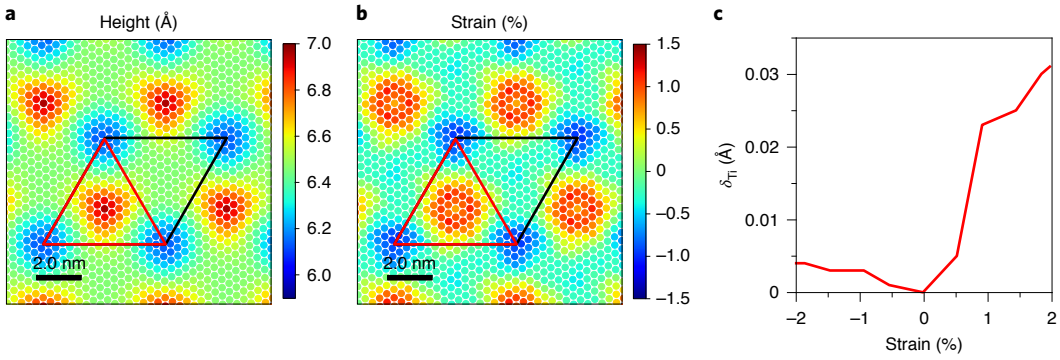

Fig. 4 | DFT calculation of the distribution of the height and strain field near a 0° twist angle. a,**b**, Relative height and local strain field of the top $TiTe_2$ layer at twist angle θ of ~1.7°. The colour bar in **a** represents the calculated height of the top $TiTe_2$ layer relative to the bottom $TiSe_2$ layer, and that in **b** represents the calculated strain value. **c**, Distortion of symmetry-inequivalent Ti atoms (δ_{Ti}) as a function of tensile strain.

neighbouring Te atoms along the in-plane direction. Figure 4b shows the calculated local strain field brought about by the atomic reconstruction. A strong tensile force is present in domain B, but almost no strain is present in domain A. Such a strain distribution is consistent with the GPA symmetric strain map $S(r)$ (Fig. 3b). In particular, the average strain strength extracted from GPA quantitatively agrees with the DFT calculations. The difference between the DFT-calculated results and the STM data is that the domains appear equilateral in Fig. 4, while those in the STM image of Fig. 3 are triangles with notably curved sides, which is mainly due to the local variations of twist angle and shear strain that are commonly present in bilayer systems. To confirm that the strain effect induces the formation of the CDW state, we calculated the distortion of symmetry-inequivalent Ti atoms[21] as a function of tensile strain in a 2×2 supercell. As shown in Fig. 4c, tension enhances atomic distortion, but compression hardly affects lattice reconstruction within the calculation error. All the calculations imply that the distribution of the local strain field is confined by the moiré pattern and produces the moiré-trapped CDW state. Similar calculations were also performed for 14.8° and 35°, as shown in Supplementary Fig. 15, in which no atomic reconstruction occurred and the local strain effect was not strong enough to induce CDW order, in good agreement with the experimental results.

Interlayer interactions have been shown to be important in other TMD CDW materials such as 1T-TaS_2 for establishing the CDW order and resulting changes in the electronic structure[27–29]. To explore whether the CDW state in the bottom $TiSe_2$ bilayer affects the formation of CDW tessellation domains in the top $TiTe_2$ monolayer, we performed additional DFT calculations with a fixed $TiSe_2$ 1×1 normal state. The results are shown in Supplementary Fig. 16. Our calculation indicates that both the CDW state and normal state $TiSe_2$ can induce a high local strain field in the $TiTe_2$ top monolayer with no prominent difference. Furthermore, the CDW tessellation of $TiTe_2$ can even be observed at room temperature, which is much higher than the critical temperature T_c of either 232 K for the $TiSe_2$ monolayer or 92 K for $TiTe_2$ (refs. [13,16]). Another recent work reported that the electronic structures are tunable by the stacking order of $TiTe_2$/$TiSe_2$, while the CDW state in the $TiTe_2$ monolayer is instead suppressed[30]. Therefore, the enhanced CDW tessellation state at a small twist angle is mainly induced by the local strain field, instead of the interlayer interactions.

Our work provides a path to tune many-body physics with twist angle moiré engineering, and the realized tessellation of alternate CDW and normal state domains may find potential in future CDW-based electronics.

Online content

Any methods, additional references, Nature Research reporting summaries, source data, extended data, supplementary information, acknowledgements, peer review information; details of author contributions and competing interests; and statements of data and code availability are available at https://doi.org/10.1038/s41563-021-01167-0.

Received: 24 January 2021; Accepted: 9 November 2021;
Published online: 16 December 2021

References

1. Bistritzer, R. & MacDonald, A. H. Moiré bands in twisted double-layer graphene. *Proc. Natl Acad. Sci. USA* **108**, 12233–12237 (2011).
2. Geim, A. K. & Grigorieva, I. V. Van der Waals heterostructures. *Nature* **499**, 419–425 (2013).
3. Dean, C. R. et al. Hofstadter's butterfly and the fractal quantum Hall effect in moiré superlattices. *Nature* **497**, 598–602 (2013).
4. Hunt, B. et al. Massive Dirac fermions and Hofstadter butterfly in a van der Waals heterostructure. *Science* **340**, 1427–1430 (2013).
5. Alden, J. S. et al. Strain solitons and topological defects in bilayer graphene. *Proc. Natl Acad. Sci. USA* **110**, 11256–11260 (2013).
6. Tong, Q. J. et al. Topological mosaics in moiré superlattices of van der Waals heterobilayers. *Nat. Phys.* **13**, 356–362 (2016).
7. Wu, F., Lovorn, T. & MacDonald, A. H. Topological exciton bands in moiré heterojunctions. *Phys. Rev. Lett.* **118**, 147401 (2017).
8. Kim, K. et al. Tunable moiré bands and strong correlations in small-twist-angle bilayer graphene. *Proc. Natl Acad. Sci. USA* **114**, 3364–3369 (2017).
9. Cao, Y. et al. Unconventional superconductivity in magic-angle graphene superlattices. *Nature* **556**, 43–50 (2018).
10. Sharpe, A. L. et al. Emergent ferromagnetism near three-quarters filling in twisted bilayer graphene. *Science* **365**, 605–608 (2019).
11. Tran, K. et al. Evidence for moiré excitons in van der Waals heterostructures. *Nature* **567**, 71–75 (2019).
12. Morosan, E. et al. Superconductivity in Cu_xTiSe_2. *Nat. Phys.* **2**, 544–550 (2006).
13. Chen, P. et al. Charge density wave transition in single-layer titanium diselenide. *Nat. Commun.* **6**, 8943 (2015).
14. Fazekas, P. & Tosatti, E. Electrical, structural and magnetic properties of pure and doped 1T-TaS_2. *Philos. Mag. B* **39**, 229–244 (1979).
15. Zhang, K. W. et al. Unveiling the charge density wave inhomogeneity and pseudogap state in 1*T*-$TiSe_2$. *Sci. Bull.* **63**, 426–432 (2018).
16. Chen, P. et al. Emergence of charge density waves and a pseudogap in single-layer $TiTe_2$. *Nat. Commun.* **8**, 516 (2017).
17. Weston, A. et al. Atomic reconstruction in twisted bilayers of transition metal dichalcogenides. *Nat. Nanotechnol.* **15**, 592–597 (2020).
18. Yoo, H. et al. Atomic and electronic reconstruction at the van der Waals interface in twisted bilayer graphene. *Nat. Mater.* **18**, 448–453 (2019).
19. Yao, Q. et al. Charge transfer effects in naturally occurring van der Waals heterostructures $(PbSe)_{1.16}(TiSe_2)_m$ ($m=1$, 2). *Phys. Rev. Lett.* **120**, 106401 (2018).

20. Lin, M. K. et al. Charge instability in single-layer $TiTe_2$ mediated by van der Waals bonding to substrates. *Phys. Rev. Lett.* **125**, 176405 (2020).
21. Guster, B., Robles, R., Pruneda, M., Canadell, E. & Ordejón, P. 2 × 2 charge density wave in single-layer $TiTe_2$. *2D Mater.* **6**, 015027 (2018).
22. Hÿtch, M. J., Snoeck, E. & Kilaas, R. Quantitative measurement of displacement and strain fields from HREM micrographs. *Ultramicroscopy* **74**, 131–146 (1998).
23. Lawler, M. J. et al. Intra-unit-cell electronic nematicity of the high-T_c copper-oxide pseudogap states. *Nature* **466**, 347–351 (2010).
24. Walkup, D. et al. Interplay of orbital effects and nanoscale strain in topological crystalline insulators. *Nat. Commun.* **9**, 1550 (2018).
25. Woods, C. R. et al. Commensurate–incommensurate transition in graphene on hexagonal boron nitride. *Nat. Phys.* **10**, 451–456 (2014).
26. Rosenberger, M. R. et al. Twist angle-dependent atomic reconstruction and moiré patterns in transition metal dichalcogenide heterostructures. *ACS Nano* **14**, 4550–4558 (2020).
27. Ritschel, T. et al. Orbital textures and charge density waves in transition metal dichalcogenides. *Nat. Phys.* **11**, 328–331 (2015).
28. Lee, S.-H., Goh, J. S. & Cho, D. Origin of the insulating phase and first-order metal-insulator transition in 1*T*−TaS_2. *Phys. Rev. Lett.* **122**, 106404 (2019).
29. Stahl, Q. et al. Collapse of layer dimerization in the photo-induced hidden state of 1T-TaS_2. *Nat. Commun.* **11**, 1247 (2020).
30. Lin, M. K. et al. Coherent electronic band structure of $TiTe_2$/$TiSe_2$ moiré bilayer. *ACS Nano* **15**, 3359–3364 (2021).

Methods

Sample preparation. The van der Waals heterostructure of $TiTe_2/TiSe_2$ was grown by MBE, with a base pressure of 1×10^{-10} mbar. First, BLG/SiC(0001) was obtained by flashing the SiC substrate up to 1,300 °C in ultrahigh vacuum a few times. Second, bilayer $TiSe_2$ was grown on the BLG/SiC(0001) substrate by coevaporating Ti (99.99%) and Se (99.999%) from Knudsen cells. The temperature of the substrate was kept at ~350 °C during $TiSe_2$ growth, with a growth rate of ~0.6 monolayers (ML) per hour. The growing surface of the $TiSe_2$/BLG/SiC was monitored in situ by reflection high-energy electron diffraction. After checking the surface quality by STM, bilayer $TiSe_2$ was adopted as the substrate for vertical epitaxy of monolayer $TiTe_2$ to form the $TiTe_2/TiSe_2$ heterostructure. Third, the $TiTe_2$ monolayer was grown by coevaporating Ti (99.99%) and Te (99.999%) onto the bilayer $TiSe_2$ substrate kept at ~370 °C, with a growth rate of ~0.6 ML h^{-1}. The growth of $TiTe_2$ was under very Te-rich conditions with a Ti/Te flux ratio of ~1:20, thus preventing possible Se–Te mixing in the growing $TiTe_2$ monolayer.

According to macroscopic measurements, such as reflection high-energy electron diffraction, the $TiTe_2$ monolayer is grown roughly with an orientation similar to that underneath the $TiSe_2$ bilayer. However, from our microscopic STM measurement, we found that in addition to those distributed in a range of twist angles near ~0° (roughly within ~±2°), $TiTe_2$ monolayer islands also exist at larger twist angles, which may be due to local thermodynamic fluctuations during epitaxial growth. By tuning the epitaxy dynamics, such as the growth rates of $TiSe_2$ and $TiTe_2$, as shown in Supplementary Fig. 3, various twist angles could be obtained. These variable local results enable us to investigate the twist-angle dependence of the CDW state.

For comparison, the $TiTe_2$ monolayer and bilayer were also directly grown on the BLG/SiC(0001) substrate by using MBE. High-purity Ti (99.99%) and Te (99.999%) were coevaporated from Knudsen cells. During growth, the substrate was kept at ~370 °C and the growth rate was ~0.6 ML h^{-1}.

STM/STS characterization. The STM and STS measurements were carried out with a low-temperature STM instrument (Unisoku USM1600) at ~4.5 K unless otherwise stated. STM topographic images were acquired under a constant current mode. STS measurements were collected with a lock-in amplifier and a typical a.c. modulation of 5–12 mV at 963 Hz.

Computational details. The DFT calculations were carried out using the Vienna Ab initio Simulation Package[31]. The pseudopotentials were constructed with the projector augmented-wave method[32,33], and the generalized gradient approximation of the Perdew–Burke–Ernzerhof type[34] was applied for the exchange–correlation potentials. A bilayer $TiTe_2$–$TiSe_2$ heterojunction slab model with 15 Å vacuum space was used to avoid possible interactions between successive slabs. In the case of structural optimization calculations, the atomic coordinates were relaxed until the energy difference between two ionic steps was below 10^{-4} eV. A Γ-only k-point mesh and a plane cut-off of 600 eV were adopted. The self-consistent energy criterion was 10^{-5} eV. The D3 method of Grimme[35] was used for van der Waals interactions between layers. In the case of non-self-consistent density of states calculations, a Γ-centred $46\times46\times1$ k-point mesh was implemented. The unfolding of band structures was performed using the Bandup[36,37] code.

Data availability

The data supporting the findings of this study are available from the corresponding authors upon reasonable request.

References

31. Kresse, G. & Hafner, J. Norm-conserving and ultrasoft pseudopotentials for first-row and transition elements. *J. Phys. Condens. Matter* **6**, 8245–8257 (1994).
32. Kresse, G. & Joubert, D. From ultrasoft pseudopotentials to the projector augmented-wave method. *Phys. Rev. B* **59**, 1758–1775 (1999).
33. Blochl, P. E. Projector augmented-wave method. *Phys. Rev. B* **50**, 17953–17979 (1994).
34. Perdew, J. P., Burke, K. & Ernzerhof, M. Generalized gradient approximation made simple. *Phys. Rev. Lett.* **77**, 3865–3868 (1996).
35. Grimme, S., Antony, J., Ehrlich, S. & Krieg, H. A consistent and accurate *ab initio* parametrization of density functional dispersion correction (DFT-D) for the 94 elements H-Pu. *J. Chem. Phys.* **132**, 154104 (2010).
36. Medeiros, P. V. C., Stafström, S. & Björk, J. Effects of extrinsic and intrinsic perturbations on the electronic structure of graphene: retaining an effective primitive cell band structure by band unfolding. *Phys. Rev. B* **89**, 041407(R) (2014).
37. Medeiros, P. V. C., Tsirkin, S. S., Stafström, S. & Björk, J. Unfolding spinor wave functions and expectation values of general operators: introducing the unfolding-density operator. *Phys. Rev. B* **91**, 041116(R) (2015).

Acknowledgements

This work was financially supported by the National Natural Science Foundation of China. W.-M.Z., L.Z., Q.-Y.L., Q.-W.W., L.-G.D., J.-G.H. and S.-C.L. acknowledge the National Natural Science Foundation of China (grant nos 11774149 and 11790311). Z.N. and S.M. acknowledge the National Natural Science Foundation of China (grant nos 91850120, 11774328 and 11934003) and the Chinese Academy of Sciences (XDB330301).

Author contributions

S.-C.L. conceived the project and designed the experiments. W.-M.Z. and L.Z. grew the epitaxial $TiTe_2/TiSe_2$ heterostructures and performed STM characterizations with the assistance of Q.-Y.L., Q.-W.W., L.-G.D. and J.-G.H.; S.-C.L. supervised the MBE growth and STM characterization. Z.N. performed the DFT calculations under the supervision of L.X. and S.M.; W.-M.Z., L.Z. and S.-C.L. wrote the manuscript with input and comments from all the authors.

Competing interests

The authors declare no competing interests.

Additional information

Supplementary information The online version contains supplementary material available at https://doi.org/10.1038/s41563-021-01167-0.

Correspondence and requests for materials should be addressed to Sheng Meng or Shao-Chun Li.

Peer review information *Nature Materials* thanks Jonas Bekaert and the other, anonymous, reviewer(s) for their contribution to the peer review of this work.